Journal of Catalysis 379 (2019) 100–111

Contents lists available at ScienceDirect

Journal of Catalysis

journal homepage: www.elsevier.com/locate/jcat

Controlling product selectivity by surface defects over MoO_x-decorated Ni-based nanocatalysts for γ-valerolactone hydrogenolysis

Guangcheng Zhang [a], Wei Li [b,*], Guoli Fan [a], Lan Yang [a], Feng Li [a,*]

[a] State Key Laboratory of Chemical Resource Engineering, Beijing Advanced Innovation Center for Soft Matter Science and Engineering, Beijing University of Chemical Technology, Beijing 100029, China
[b] SINOPEC Beijing Research Institute of Chemical Industry Yanshan Branch, Beijing 102500, China

ARTICLE INFO

Article history:
Received 17 May 2019
Revised 12 September 2019
Accepted 16 September 2019

Keywords:
Surface detective structure
Selective hydrogenolysis
Cooperative action
Nickel nanoparticles

ABSTRACT

Currently, highly efficient biomass upgrading over non-noble metal catalysts is of vital importance for reducing equipment and operation expenses in biorefinery industries. In this respect, the related heterogeneous catalysis demands the design and construction of mutual cooperative microstructure of catalysts to improve their catalytic performances. Here, an efficient catalytic process for selective hydrogenolysis of biomass-derived γ-valerolactone (GVL) to produce 1,4-pentanediol (1,4-PDO) and 2-methyltetrahydrofuran (2-MTHF) was developed by earth-abundant nickel-based catalysts, which were derived from a molybdate intercalated Ni-Al layered double hydroxide precursor. It was found that with the elevated reduction temperature, the amount of surface defective MoO_x species ($0 < x < 3$) was gradually increased. Especially, as-fabricated Ni-MoO_x/Al_2O_3 catalyst obtained at the reduction temperature of 600 °C delivered a 94.0% combined yield of 1,4-PDO and 2-MTHF under mild reaction conditions. It was demonstrated that over the present Ni-MoO_x/Al_2O_3 catalyst system, surface defective MoO_x species could greatly facilitate the adsorption and activation of carbonyl group in GVL and thus significantly promote the cleavage of C═O bond and its adjacent C—O bond. This finding opens a promising door to engineer surface defective structure of high-performance supported metal catalysts.

1. Introduction

Over the past decade, with the depletion and increasing consumption of fossil resources, catalytic conversion of abundant and renewable biomass resources for producing a handful of important chemicals and liquid biofuels, as well as reducing the related waste in agricultural and food industries, is gaining a lot of attention [1–3]. In this respect, lignocellulose-derived levulinic acid (LA) is becoming the most important plat molecule as a vital resource of C5 compound for producing γ-valerolactone (GVL), 1,4-pentanediol (PDO), 2-methyltetrahydrofuran (2-MTHF) and alkanes [4–8]. Among them, 1,4-PDO, an attractive highly valuable biogenic diol, can be used as a building block to synthesize high-performance biodegradable polyesters, thermoplastics and polyurethanes [9,10], while 2-MTHF is also considered as a part of P-series fuel or applied as a versatile solvent in the pharmaceutical industry [11,12].

Previously, it was reported that noble metals (*e.g.* Pt [13], Pd [14], Ru [9,15], and Rh [9]) were active as catalysts in liquid phase LA hydrogenation to generate 1,4 PDO under high hydrogen pressures (>5 MPa). Despite high yields (>90%) in some cases, high cost and resource scarcity of noble metals always limit their large-scale industrial applications. Recently, Ru-[16,17], Fe-[18] and Co-based [19,20] molecular catalyst systems also have been applied in the conversion of another significant cellulose-derived GVL into 1,4-PDO, despite some drawbacks including special handling of metal complexes, difficulty in separation and reusability of catalysts, and their high cost. In addition, some heterogeneous non-noble copper-based catalysts were reported to catalyze the GVL hydrogenation to produce 1,4-PDO [12,21–23]. Especially, Cu/ZrO_2 catalyst could afford a 95% yield of 1,4-PDO at 200 °C and 6 MPa hydrogen pressure [12]. Nevertheless, due to the inherent chemical stability of GVL, conversion of GVL needs to be performed under relatively harsh reaction conditions. Therefore, the investigation of heterogeneous non-noble metal catalytic systems for high-efficiency GVL hydrogenolysis is quite worthwhile.

Layered double hydroxides (LDHs, $[M^{2+}_{1-x}M^{3+}_x(OH)_2]^{x+}[A_{x/n}]^{n-}\cdot mH_2O$), known as a class of two-dimensional multi-metal layered materials, possess uniform distribution of different divalent and trivalent cations on the brucite-like layers [24,25]. More interestingly, various metal complex anions can be intercalated into their

* Corresponding authors.
E-mail addresses: liweisea@sina.com (W. Li), lifeng@mail.buct.edu.cn (F. Li).

https://doi.org/10.1016/j.jcat.2019.09.021
0021-9517/

interlayer space, constructing a host-guest supramolecular structure. Such structural flexibility and versatility of LDHs make them promising catalyst precursors. Correspondingly, a variety of readily available, highly active, and stable supported metal catalyst systems can be fabricated through structural transformation [26–30]. Recently, we have reported highly dispersive Ni-based catalysts derived from Ni-containing LDH precursors for efficiently catalyzing the selective hydrogenation of LA to GVL using molecular hydrogen [3].

In this work, we developed a new MoO_x-decorated Ni-based catalyst system for liquid-phase selective hydrogenolysis of GVL to produce 1,4-PDO and 2-MTHF, which was derivable from a molybdate ($Mo_7O_{24}^{6-}$) intercalated NiAl-LDH precursor. By adjusting the reduction temperature of catalyst precursors, the generation of surface defective MoO_x species (*i.e.* low-coordinated molybdenum-oxygen vacancy pairs) was governed. It was demonstrated that efficiently controlling the adsorption and activation of carbonyl group in GVL by surface defective MoO_x species could significantly promote the selective cleavage of C=O bond and its adjacent C-O bond of ester group in GVL to generate 1,4-PDO and 2-MTHF. The present work provides a representative example for efficiently modulating the surface defective structure of Ni-based catalysts, thus rationally governing the activation of reactant molecules and enhancing the selectivity of desired products in the upgrading of biomass-derived oxygenates.

2. Experimental

2.1. Catalyst preparation

Nitrate-type NiAl-LDH was prepared by a traditional coprecipitation method. First, $Ni(NO_3)_2{\cdot}6H_2O$ (0.04 mol) and $Al(NO_3)_3{\cdot}9H_2O$ (0.02 mol) were dissolved in 100 ml of decarbonated deionized water. Subsequently, the above salt solution was titrated by NaOH solution (1.2 M) under vigorous agitation under nitrogen atmosphere at room temperature, until the pH value reaches 8.0. The resulting suspension was aged at 70 °C for 24 h under nitrogen atmosphere, centrifuged and washed with decarbonated deionized water for several times to obtain NiAl-NO_3-LDH sample.

Molybdate intercalated NiAl-LDH precursor (NiAl-Mo_7O_{24}-LDH) was prepared by an ion-exchange method. First, NiAl-NO_3-LDH was dispersed into 100 ml of decarbonated deionized water. Subsequently, $(NH_4)_6Mo_7O_{24}{\cdot}4H_2O$ (0.04 mol) was dissolved in 100 ml of decarbonated deionized water. Then the salt solution was titrated by LDH dispersion solution under vigorous agitation and nitrogen atmosphere at room temperature. Meanwhile, the pH value of the solution was controlled at 5.0 ± 0.2 by dilute nitric acid (0.2 M). After titration, the resulting suspension was aged at 70 °C for 18 h and centrifuged. The precipitate was washed with decarbonated deionized water for several times and dried at 70 °C overnight under vacuum to obtain NiAl-Mo_7O_{24}-LDH. Then NiAl-Mo_7O_{24}-LDH was calcined in static air at 500 °C for 4 h to obtain Ni-Mo-Al mixed metal oxide (denoted as NiMoAl-MMO). Finally, NiMoAl-MMO put into the quartz tube was reduced in a 10% (v/v) H_2/Ar flow at 400, 500 and 600 °C at a ramping rate of 2 °C/min and held for 4 h to obtain reduced Ni-MoO_x/Al_2O_3-400, Ni-MoO_x/Al_2O_3-500 and Ni-MoO_x/Al_2O_3-600 samples. After cooling to room temperature, the quartz tube was filled with nitrogen and the obtained reduced Ni-based catalyst was placed in a glove box and sealed in a sample tube filled with N_2 to prevent reduced samples from being exposed to air before characterization and reactions. For comparison, carbonate-type NiAl-LDH (NiAl-CO_3-LDH) was prepared according to the identical procedure to that for NiAl-NO_3-LDH in the presence of a mixed base solution of NaOH (1.2 M) and Na_2CO_3 (0.6 M). NiAl-CO_3-LDH was calcined and reduced according to the identical procedure to that for Ni-MoO_x/Al_2O_3-500. The calcined NiAl-CO_3-LDH was denoted as NiAl-MMO, while the reduced NiAl-MMO was denoted as Ni/Al_2O_3-500. In addition, commercial Al_2O_3 and MoO_3 (99%, Alfa Aesar) supported Ni catalysts (im-Ni/Al_2O_3 and im-Ni/MoO_3) with the Ni loading of about 35% were prepared by an incipient wetness impregnation method.

2.2. Characterization

X-ray diffraction (XRD) patterns were obtained on a Shimadzu XRD-6000 diffractometer with Cu Ka radiation. The metal content was analyzed on Shimadzu ICPS-75000 inductively coupled plasma emission spectrometer (ICP–AES). Raman spectra of samples were collected from a microscopic confocal Raman spectrometer (Jobin Yvon Horiba HR800) using Ar^+ laser of 514 nm wavelength as the excitation source. Fourier transform infrared (FTIR) spectra were recorded on a Bruker Vector-22 spectrometer. Low temperature N_2 adsorption-desorption experiments were conducted on Micromeritics ASAP 2020 absorptometer. X-ray photoelectron spectra (XPS) were recorded from a Thermo VG ESCALAB 250 X-ray photoelectron spectrometer using Al Ka X-ray of 1486.6 eV. The microstructure of samples was determined using transmission electron microscopy (HRTEM, JEOL2100). Positron annihilation spectroscopy (PAS) was carried out on a fast/slow coincidence ORTEC system in the transmission mode using ^{22}Na as the radioactive positron source at Beijing Synchrotron Radiation Facility. Temperature programmed decomposition (TPDE), H_2 temperature-programmed reduction (H_2-TPR) and H_2 temperature-programmed desorption (H_2-TPD) of the samples were conducted on Micromeritics ChemiSorb 2920 using a thermal conductivity detector (TCD). For H_2-TPR, the sample (100 mg) was degassed under Ar flow at 200 °C for 2 h to remove adsorbed water on the surface. During H_2-TPR process, a cold trap was applied to remove the formed water due to the reduction, and the temperature of cold trap was set below −88.5 °C by mixing liquid nitrogen with isopropanol. Afterwards, TPR measurement was performed in a flow of 10% H_2/Ar (30 ml min^{-1}) with a heating rate of 10 °C min^{-1} from 50 to 900 °C. For TPDE, NiMoAl-MMO (100 mg) was reduced in a flow of H_2/Ar gas of 10% H_2/Ar (50 ml min^{-1}) at 400 °C and was degassed under Ar flow at 200 °C for 2 h. Afterward, the temperature was raised from 50 to 900 °C under Ar flow at a ramping rate of 10 °C min^{-1}. For H_2-TPD, the sample (100 mg) was reduced in a flow of H_2/Ar gas of 10% H_2/Ar (50 ml min^{-1}) at a certain reduction temperature and was degassed under Ar flow at 200 °C for 2 h. After that, the reduced sample was treated in a flow of H_2/Ar gas mixture and held for 2 h at 25 °C. Finally, chemisorbed H_2 was desorbed in a flow of Ar at a ramping rate of 10 °C min^{-1}. In addition, H_2-TPD experiments using mass spectrometer detector (UK HIDEN QIC-20) also were carried out under the identical procedure to that for H_2-TPD experiments using TCD detector·NH_3-TPD experiments were performed using a chemical adsorption instrument (Thermo Fisher TPDRO-1100). In situ FTIR spectra of GVL adsorbed on samples were obtained on a Nicolet 380 type spectrophotometer. First, the pressed thin slice sample was placed into an IR cell and heated to 200 °C and held for 1 h under nitrogen atmosphere. After cooling to 25 °C, GVL was introduced and balanced for 2 h. Finally, FTIR spectra were recorded under vacuum. H_2 pulse chemisorption was conducted using a Micrometric ChemiSorb 2920 chemisorption instrument Oxygen consumption amount (OC, mol/g) of Ni-based samples was obtained via oxygen pulse injection method. First, the reduced sample was purged in a He flow (40 ml/min) and heated to 200 °C for 0.5 h. After cooling to 25 °C, a mixed O_2/He flow (1:9, v/v) was injected periodically until the oxygen signal kept unchanged. Considering that an oxygen atom to metallic Ni atom stoichiometric factor is 1:1, the amount

of surface oxygen vacancies (C_v, mol/g) may be obtained based on to the following equation:

$$C_V = OC - H_2 uptake$$

where H_2 uptake is moles of desorbed H_2 per unit mass of the reduced sample by determined H_2 pulse chemisorption.

2.3. Catalyst test

In a typical run, the batch autoclave reactor was loaded with the catalyst (0.1 g), GVL (10 mmol), and mesitylene (20 ml), and then sealed and flushed with pure H_2 10 times. After being placed in a heating jacket and preheated to the certain temperature, the autoclave was charged with H_2 to a certain pressure and with stirring at a speed of 1000 rpm. After the reaction, the reactants were cooled rapidly in an ice bath, and the reaction mixture was filtered and quantitatively analyzed by gas chromatograph (Agilent 7890B) equipped with a DB-WAX capillary column (30.0 m × 250 μm × 0.25 μm) and a flame ionization detector using dioxane as an internal standard substance. The spent catalyst was recovered from the reaction solution by centrifugation and washed several times with deionized water and ethanol before the next cyclic test.

3. Results and discussion

3.1. Structural analysis of samples

The crystalline structures of different NiAl-CO_3-LDH, NiAl-NO_3-LDH and NiAl-Mo_7O_{24}-LDH precursors were characterized by XRD. As shown in Fig. 1A, XRD patterns of NiAl-CO_3-LDH present characteristic (0 0 3), (0 0 6) and (0 1 2) diffractions of hydrotalcite-like materials. The diffractions at about 11.7° correspond to the basal spacing of approximately 0.754 nm, in good line with the reported value for carbonate-intercalated NiAl-LDH [26]. In two cases of NiAl-NO_3-LDH and NiAl-Mo_7O_{24}-LDH, the characteristic (0 0 3) diffraction of LDH phase obviously shifts to about 9.8° and 8.2°, respectively. Consequently, the basal spacing is increased to approximately 0.879 nm for NiAl-NO_3-LDH or 1.074 nm for NiAl-Mo_7O_{24}-LDH, characteristic of the typical feature of nitrate or molybdate intercalated LDH materials reported in the literature [31,32]. Clearly, FT-IR spectra of NiAl-NO_3-LDH and NiAl-Mo_7O_{24}-LDH precursors indicate characteristic absorption bands of interlayer Mo-oxygen bond (822 cm^{-1} for the v_4 vibration) and nitrate ions (1383 cm^{-1} for v_3 vibration and 836 cm^{-1} for v_2 vibration) [33–35] (Fig.S1). Meanwhile, Raman spectrum of NiAl-Mo_7O_{24}-LDH (Fig.S2) depicts three vibration peaks around 352, 910 and 3629 cm^{-1}, respectively, which are attributable to the bending vibration of the Mo=O bond, the symmetrical vibration of the Mo-O bond and the stretching vibration of Mo-OH [32,35], respectively. No vibration peaks related to carbonate and nitrate ions can be observed. The above results confirm that interlayer nitrate ions in NiAl-LDH can be successfully exchanged by $Mo_7O_{24}^{6-}$ ion, finally forming $Mo_7O_{24}^{6-}$ intercalated NiAl-LDH.

After calcination of NiAl-CO_3-LDH and NiAl-Mo_7O_{24}-LDH precursors at 500 °C, XRD patterns of NiAl-MMO and NiMoAl-MMO present characteristic diffractions of NiO phase (JCPDS no. 44-1159) and/or $NiMoO_4$ phase (JCPDS no. 12-0348) (Fig.S3), due to the collapse and decomposition of the initial layered structure of LDH precursors upon heat treatment. However, in two cases, no crystalline Al_2O_3 phases can be detected, due to the formation of the high dispersive amorphous alumina. Further, the reduced samples were analyzed by XRD (Fig. 1B). Notably, for Mo-free Ni/Al_2O_3-500, only three characteristic diffractions corresponding to the (1 1 1), (2 0 0) and (2 2 0) crystal planes of metallic Ni appear. In the cases of Ni-MoO_x/Al_2O_3-400, Ni-MoO_x/Al_2O_3-500 and Ni-MoO_x/Al_2O_3-600, in addition to those of metallic Ni, several diffraction peaks corresponding to molybdenum oxides (*e.g.* MoO_3 and/or MoO_2) can be detected, indicative of the decomposition of molybdate anion and/or the further reduction of Mo^{6+} species. In all cases, the Ni/Al molar ratio in reduced Ni-based samples is close to 2:0 based on the ICP-AES analysis. The structural and compositional data of samples are summarized in Table 1. In all cases, the average size of resultant Ni^0 particles in Ni-MoO_x/Al_2O_3 samples was estimated to be *ca.* 10.8–12.4 nm based on Scherrer equation analyses. Especially, Ni-MoO_x/Al_2O_3-500 sample possesses a higher BET surface area than the other two Ni-MoO_x/Al_2O_3-400 and Ni-MoO_x/Al_2O_3-600 samples, which is lower than that of Ni/Al_2O_3-500 sample.

Further, the microstructure of the representative Ni-MoO_x/Al_2O_3-500 sample was determined through TEM observation. As shown in Fig. 2, the sample is composed of many small nanoparticles (NPs) of about 10 nm in size, which form a highly hybrid microstructure, besides few aggregates of NPs. HRTEM image reveals three clear lattice spacings of about 0.203, 0.236 and

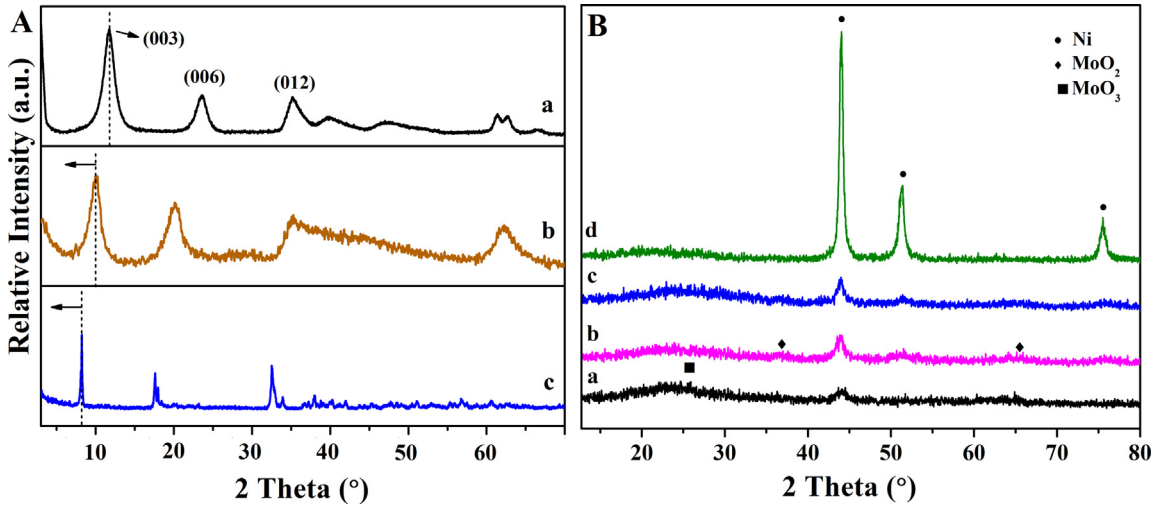

Fig. 1. XRD patterns (A) of NiAl-CO_3-LDH (a), NiAl-NO_3-LDH (b) and NiAl-Mo_7O_{24}-LDH (c) precursors, and XRD patterns (B) of Ni-MoO_x/Al_2O_3-400 (a), Ni-MoO_x/Al_2O_3-500 (b), Ni-MoO_x/Al_2O_3-600 (c) and Ni/Al_2O_3-500 (d).

Table 1
The compositional and structural properties of samples.

Samples	Ni [a] (wt %)	Mo [a] (wt %)	S_{BET} [b] (m^2/g)	Vp [c] (cm^3/g)	Dp [d] (nm)	D_{111} [e] (nm)	D_{SA} [f] (mmol/g)
Ni-MoO_x/Al_2O_3-400	34.6	31.9	74	0.08	4.8	11.7	1.428 (0.457) [g]
Ni-MoO_x/Al_2O_3-500	36.1	33.8	93	0.13	4.6	10.8	2.077 (0.717)
Ni-MoO_x/Al_2O_3-600	38.3	35.6	64	0.14	6.1	12.4	1.593 (0.601)
Ni/Al_2O_3-500	66.3	0	117	0.65	15.3	9.2	1.358 (0.458)

[a] Determined by ICP-AES.
[b] Specific surface area calculated by the BET method.
[c] Total pore volume.
[d] Average pore size based on BJH method.
[e] Average crystallite size of Ni particles estimated from XRD patterns.
[f] Density of total acidic sites determined by NH_3-TPD.
[g] Data in parentheses show the density of moderate strength acidic sites corresponding to the desorption in the region of 200–500 °C.

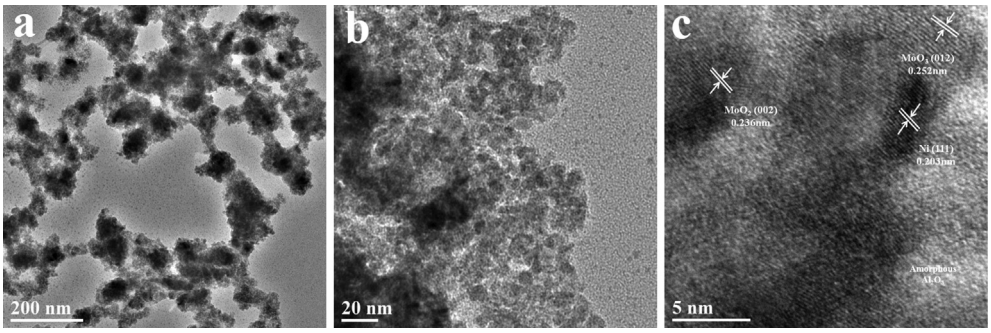

Fig. 2. TEM (a) and HRTEM (b,c) images of the representative Ni-MoO_x/Al_2O_3-500 sample.

0.252 nm assigned to the (1 1 1), (0 0 2), and (0 1 2) planes of metallic Ni, MoO_2 and MoO_3 phases, respectively. Meanwhile, amorphous alumina is distributed in the region between the above three crystalline phases. The results illustrate the uniformly dispersed state of different components on the surface of Ni-MoO_x/Al_2O_3-500 sample.

3.2. Surface properties of samples

To gain surface chemical states of samples, reduced Ni-based samples were characterized by XPS analysis. As shown in Fig. 3A, in fine Ni 2p spectra of reduced Ni-based samples, six fitted bands at about 852.7, 856.0, 861.6, 869.9, 873.4 and 879.3 eV are associated with Ni $2p_{3/2}$ and Ni $2p_{1/2}$ core levels of both metallic Ni^0 and Ni^{2+} species as well as with satellite peaks from Ni^{2+} species, respectively [36,37]. Further, according to the integrated areas of two kinds of Ni species, the relative proportion of surface Ni^0 species in the total Ni component increases gradually with the increasing reduction temperature (Table 2). In all cases, the presence of large amounts of surface Ni^{2+} species may due to re-oxidization of surface partial Ni^0 species after preparation and exposure to air. As shown in Fig. 3B, in the fine Mo 3d spectrum

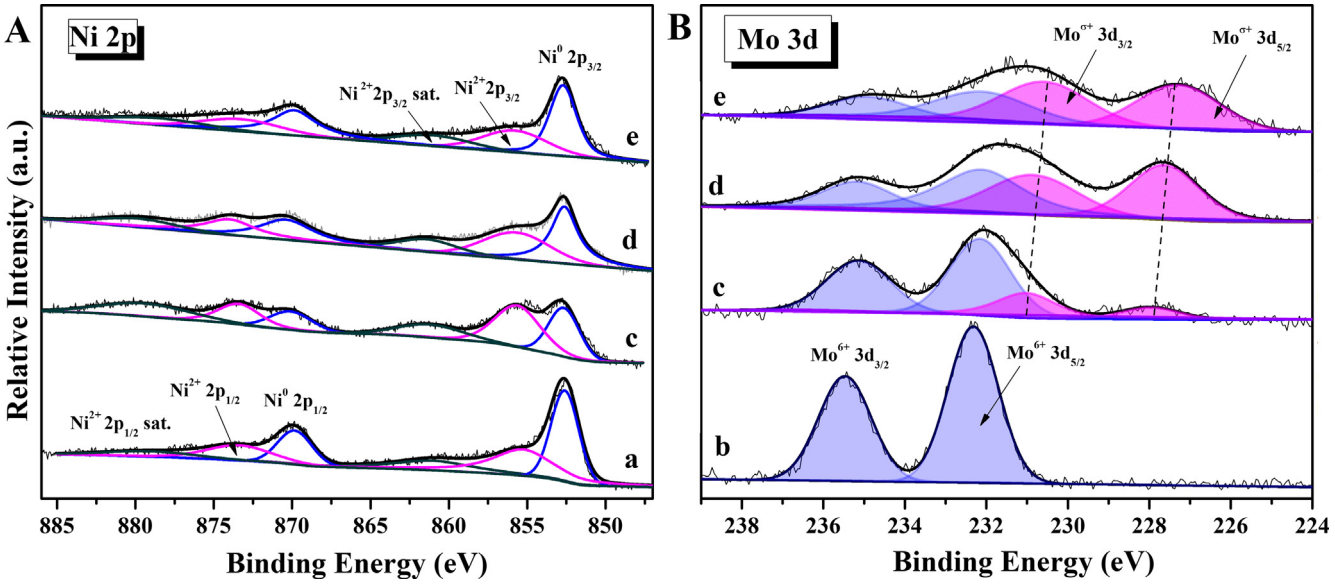

Fig. 3. XPS of Ni 2p (A) and Mo 3d (B) regions for Ni/Al_2O_3-500 (a), NiMoAl-MMO (b), Ni-MoO_x/Al_2O_3-400 (c) Ni-MoO_x/Al_2O_3-500 (d) and Ni-MoO_x/Al_2O_3-600 (e) samples.

Table 2
The surface defective data of samples.

Samples	BE of $Mo^{\sigma+}$ [a] (eV)	$Mo^{\sigma+}/(Mo^{\sigma+}+Mo^{6+})$ ratio [c]	$Ni^0/(Ni^{2+}+Ni^0)$ ratio [c]	$O_{II}/(O_{II}+O_I)$ ratio [c]	Cv [d] (μmol/g)
Ni-MoO_x/Al_2O_3-400	228.0 (231.0) [b]	0.17	0.42	0.32	72.6
Ni-MoO_x/Al_2O_3-500	227.6 (230.8)	0.54	0.55	0.38	165.9
Ni-MoO_x/Al_2O_3-600	227.3 (230.6)	0.63	0.63	0.46	226.2
Ni-MoO_x/Al_2O_3-700	227.1 (230.3)	0.66	0.68	0.50	175.3
Ni/Al_2O_3-500	–	–	0.53	0.15	5.2

[a] Binding energy of $Mo^{\sigma+}$ species ($0 < \sigma < 6$) in the Mo 3d $_{5/2}$ region determined from XPS results.
[b] Values in parentheses are BE of $Mo^{\sigma+}$ species in Mo 3d $_{3/2}$ region.
[c] Determined by Mo 3d, Ni 2p or O 1s regions of XPS results.
[d] Determined by using the oxygen pulse injection method.

of NiMoAl-MMO, two XPS peaks appear at about 232.3 eV and 235.7 eV, which can be ascribed to the 3d $_{5/2}$ and 3d $_{3/2}$ of Mo^{6+} species [38–40], respectively, indicating that Mo species mainly exist in the form of MoO_3 phase in the NiMoAl-MMO. After reduction at 400 °C, two main Mo^{6+} peaks become broad and another two fitted small peaks appear at about 228.0 eV and 231.0 eV, respectively. It demonstrates that a part of Mo^{6+} species is reduced to $Mo^{\sigma+}$ species ($4 < \sigma < 6$) [41]. With the further increase in the reduction temperature to 500 °C and 600 °C, the peak intensities for Mo^{6+} species are gradually reduced, while the peak intensities for $Mo^{\sigma+}$ species are enhanced and the peaks shift to lower binding energies of about 227.3 and 230.5 eV for Mo $3d_{5/2}$ and Mo $3d_{3/2}$ core levels. It illustrates that the higher reduction temperature of 600 °C may lead to the formation of $Mo^{\sigma+}$ species with lower valence states ($0 < \sigma \leq 4$). Previously, it also was reported that MoO_3 species could be partially reduced to MoO_x with oxygen vacancy (O_v) by activated hydrogen atoms migrated from active metallic species through hydrogen spillover [13,42]. The above results demonstrate that the Mo^{6+} species in the calcined sample can be partially reduced at higher reduction temperatures, and the reduction degree of Mo species is increased with the reduction temperature, thereby resulting in the formation of large amounts of MoO_x species on the catalyst surface.

In order to further investigate the effect of the introduction of Mo species on the surface structure of reduced samples, the fine O 1s spectra of different reduced Ni-based samples were analyzed. As shown in Fig. 4, there are two peaks at about 530.1 and 531.7, respectively, which are attributed to the lattice oxygen species (O^{2-}) and defective oxides or adsorbed hydroxyl species originating from surface oxygen vacancies [43–45]. Another small peak at 535.5 eV is mainly assigned to surface adsorbed water molecules. Compared with Ni/Al_2O_3-500 sample, reduced Ni-MoO_x/Al_2O_3 samples exhibit higher $O_{II}/(O_I + O_{II})$ ratios, which are progressively increased with the reduction temperature, indicative of the formation of more oxygen vacancies due to the reduction of Mo^{6+} species and thus the loss of lattice oxygen (Mo^{6+}–O^{2-}–$Mo^{6+} + H_2 \rightarrow Mo^{\sigma+}$–$O_v$–$Mo^{\sigma+} + H_2O$). The above results confirm that the reduction of Mo^{6+} species at higher temperatures can lead to the formation of more surface oxygen vacancies and defective MoO_x species. In addition, to determine surface acidity of samples, NH_3-TPD experiments were carried out. As shown in Fig.S4, Ni-MoO_x/Al_2O_3-500 especially exhibits larger amounts of total and moderate strength acidic sites (Table 1), probably due to its higher surface area, as well as the presence of a large amount of low-valent molybdenum sites acting as surface Lewis acid sites.

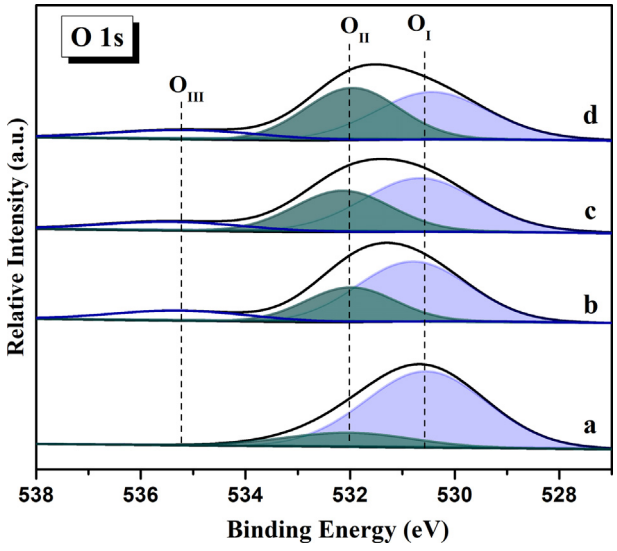

Fig. 4. XPS of O1s region for Ni/Al_2O_3-500 (a) Ni-MoO_x/Al_2O_3-400 (b) Ni-MoO_x/Al_2O_3-500 (c) and Ni-MoO_x/Al_2O_3-600 (d) samples.

In order to detect the dimension and contents of free-volume holes in solids, positron annihilation spectra (PAS) also was measured in low-density regions around dislocations or vacancies. Table 3 shows three distinct kinds of positron lifetime components (τ_1, τ_2, and τ_3) with the relative intensities over different samples. Among them, the component with the shortest lifetime (τ_1) is assigned to small bulk defects of particles (*e.g.*, monovacancies) [46,47], while the τ_2 component is associated with large vacancy clusters on the surface boundary and the interface of particles. In addition, the component with the longest lifetime (τ_3) is related to intercrystallite spaces. Notably, the intensity of τ_2 component for Mo-containing reduced samples, as well as the relative intensity ratio of τ_2 component to τ_1 component, is higher than that for Mo-free Ni/Al_2O_3-500 and increases with the reduction temperature. It further demonstrates that the sample reduced at the higher temperature of 600 °C possesses more abundant oxygen vacancies, well consistent with the XPS results. Meanwhile, we quantitatively analyzed the content of oxygen vacancies by O_2-pulse adsorption [48]. It is found from Table 2 that the content of oxygen vacancies in the Ni/Al_2O_3-500 sample is very low. For Ni-MoO_x/Al_2O_3 samples, the adsorption capacity for oxygen is dramatically increased with the elevated reduction temperature from 400 to 600 °C. However, the amount of surface oxygen vacancies (C_v value) on the Ni-MoO_x/Al_2O_3-700 with a lower specific surface area of 14 m^2/g is smaller than that on the Ni-MoO_x/Al_2O_3-600, mainly due to the sintering of the sample at the higher reduction temperature of 700 °C. The above results further confirm that abundant surface oxygen vacancies can be formed on the Ni-MoO_x/Al_2O_3 samples by the introduction of Mo species and the regulation of the reduction temperature.

H_2-TPR characterization was performed to investigate the redox properties of calcined samples. As shown in Fig. 5, in addition to three small reduction peaks related to the reduction of surface Ni^{3+} species in Ni_2O_3 (376 °C), highly dispersed Ni^{2+} species in NiO (516 °C), and spinel-type $NiAl_2O_4$ phase (819 °C), NiAl-MMO

Table 3
The PAS data of different samples.

Sample	τ_1 (ns)	τ_2 (ns)	τ_3 (ns)	I_1 [a] (%)	I_2 [a] (%)	I_3 [a] (%)	I_2/I_1 [b]
Ni/Al_2O_3-500	0.2015	0.3810	2.785	47.0	51.4	1.59	1.09
Ni-MoO_x/Al_2O_3-400	0.1477	0.3550	2.459	44.7	53.5	1.76	1.19
Ni-MoO_x/Al_2O_3-500	0.1796	0.3912	3.094	39.6	58.3	2.19	1.47
Ni-MoO_x/Al_2O_3-600	0.1848	0.3787	2.558	35.9	62.1	2.05	1.72

[a] Proportions of different components.
[b] Relative intensity ratio of the τ_2 component to the $\tau_1$component.

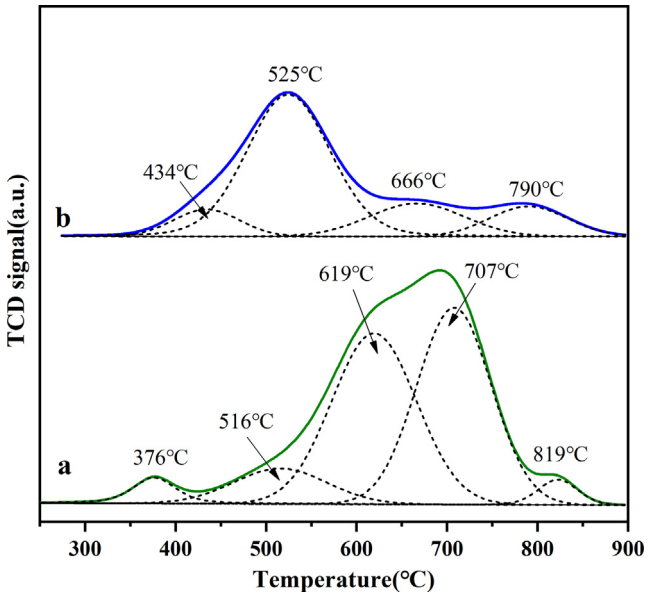

Fig. 5. H_2-TPR profiles of NiAl-MMO (a) NiMoAl-MMO (b) samples.

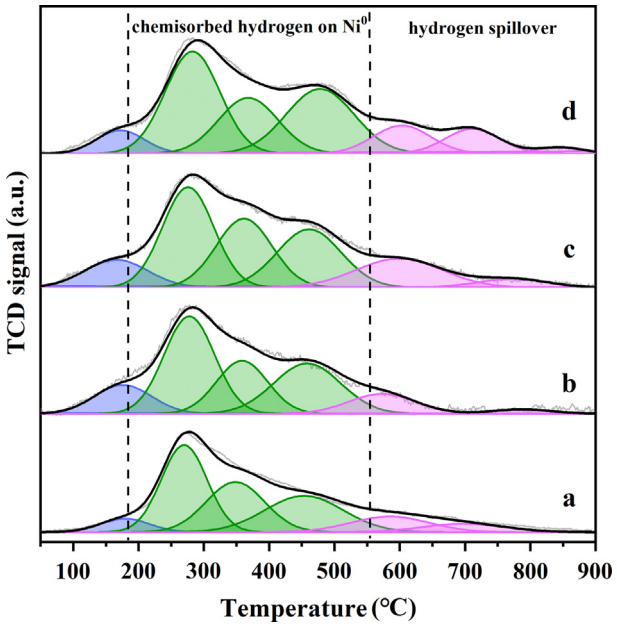

Fig. 6. H_2-TPD profiles of Ni/Al_2O_3-500 (a), Ni-MoO_x/Al_2O_3-400 (b), Ni-MoO_x/Al_2O_3-500 (c) and Ni-MoO_x/Al_2O_3-600 (d) samples.

sample exhibits a broad and strong reduction region with two fitted peaks at 619 and 707 °C, due to the reduction of bulk NiO phase [49]. In the case of NiMoAl-MMO, the main reduction peak related to Ni^{2+} species in bulk $NiMoO_4$ negatively shifts to 520 °C, demonstrating that the introduction of Mo species can weaken the interaction between Ni-containing species and the support and improve the dispersion of Ni species. Meanwhile, the reduction of cationic Mo^{6+} species to $Mo^{\sigma+}$ species with the lower chemical valences also appears in the range of 600–750 °C [50–52]. Based on the above H2-TPR results, the hydrogen consumption of NiMoAl-MMO is about 14.7 mmol/g, which is less than that of NiAl-MMO (23.2 mmol/g), due to a lower Ni content of about 30.2 wt% in the NiMoAl-MMO than that in the NiAl-MMO (about 58.7 wt%), as well as the incomplete reduction of Mo^{6+} species.

Usually, active metallic sites over supported metal catalysts play a key role in the dissociation of the hydrogen molecule in the hydrogenation process. To investigate the interactions between metallic sites and hydrogen species, as well as the surface structural property of supports, H_2-TPD experiments were conducted (Fig. 6). In addition, there is no obvious detective TCD signal in the range of 50–900 °C in the TPDE curve of the representative Ni-MoO_x/Al_2O_3-400 (Fig.S5). Also, as shown in the Fig.S6, the TCD curve of representative Ni/Al_2O_3-500 and Ni-MoO_x/Al_2O_3-600 samples in the H_2-TPD process in the temperature range of 50–900 °C is in good agreement with the only signal for desorbed hydrogen determined by mass spectrometer detector. Combining with the above blank TPD without hydrogen adsorption and H_2-TPD-MS results (Fig.S5 and Fig.S6), it can be concluded that the present TCD signals of Ni-based catalysts in the H_2-TPD process can represent the hydrogen desorption on Ni-based samples. All reduced Ni-based samples present a small desorption associated with surface weak adsorption of hydrogen in the temperature range of 50–200 °C. The release of chemisorbed hydrogen on Ni^0 atoms in the broad range of 200 to 550 °C is assigned to the desorption of hydrogen from terrace to step and then to the corner sites of Ni^0 [53–55], while the desorption above 550 °C is attributed to hydrogen spillover from metals on the support [55,56]. In comparison, Ni-MoO_x/Al_2O_3-700 sample was further prepared by the reduction of NiMoAl-MMO at 700 °C. TEM images reveal the serious agglomeration of Ni particles on the Ni-MoO_x/Al_2O_3-700 surface (Fig.S7), while the H_2-TPD result indicates a smaller density of exposed Ni^0 sites than those of Ni-MoO_x/Al_2O_3-500 and Ni-MoO_x/Al_2O_3-600 samples (Fig.S8 and Table 4).

In our present catalyst system, although Ni/Al_2O_3-500 sample possesses more metallic exposed Ni sites than Ni-MoO_x/Al_2O_3-400 or approximate value to that of Ni-MoO_x/Al_2O_3-500 (Table 4), the amount of surface oxygen vacancies on the Ni/Al_2O_3-500 is much less than those on other Ni-MoO_x/Al_2O_3 samples (Table 2). Further, the XPS results of Ni-MoO_x/Al_2O_3-700 sample reveal the formation of the largest surface $Mo^{\sigma+}/(Mo^{\sigma+} + Mo^{6+})$ molar ratio among all Ni-MoO_x/Al_2O_3 catalysts (Fig.S9), indicative of the increased surface fraction of $Mo^{\sigma+}$-O_v-$Mo^{\sigma+}$ structure. The above results demonstrate that the surface oxygen vacancy on Ni-based samples has no relevance to the number of surface metallic Ni sites. Meanwhile, the concentration of spillover hydrogen does not increase linearly with the number of exposed Ni^0 sites, indicating that besides metallic Ni sites, the surface structure of catalysts, such as surface acidity and surface defects, can affect the hydrogen spillover. It is inferred that the significant hydrogen spillover for

Table 4
Data of H_2 desorption and TOF values over Ni-based samples.

Samples	H_2 uptake (mmol/g)	H_{Ni}[a] (mmol/g)	H_{sp}[b] (mmol/g)	TOF_{GVL}[c] (h^{-1})	$TOF_{PDO+MTHF}$[d] (h^{-1})
Ni-MoO_x/Al_2O_3-400	0.301	0.233	0.033	36.1	15.6
Ni-MoO_x/Al_2O_3-500	0.388	0.281	0.069	63.6	41.7
Ni-MoO_x/Al_2O_3-600	0.461	0.348	0.084	71.5	52.6
Ni-MoO_x/Al_2O_3-700	0.373	0.254	0.075	68.5	55.5
Ni/Al_2O_3-500	0.347	0.275	0.053	43.5	9.0

[a] Desorption in the range of 200–550 °C.
[b] Desorption in the range of 500–900 °C.
[c] Calculated based on the moles of GVL converted per mole surface metallic nickel (mole number of exposed surface metallic nickel was determined by H_2-TPD) in the initial 15 min.
[d] Calculated based on the moles of 1,4-pentanediol and 2-methyltetrahydrofuran produced per mole surface metallic nickel determined by H_2-TPD in the initial 15 min.

Ni-MoO_x/Al_2O_3-600 may be assigned to the abundant defective sites, as well as an appropriate amount of surface acidic sites.

3.3. Catalytic performance of catalysts

As shown in Scheme 1, the GVL hydrogenolysis can be carried out mainly through three pathways. In general, GVL is more susceptible to the cleavage of the C-O bond at the position (1) to produce pentenoic acid (PA) [57–59], followed by rapid hydrogenation to form valeric acid (VA). Meanwhile, the selective hydrogenolysis through the cleavage of the C-O bond or C=O bond of ester group at positions (2) or (3) in GVL can produce 1,4-PDO or 2-MTHF, which may be mainly regulated by delicately designing the structure of catalysts, as well as controlling the reaction conditions. Specially, the cleavage of the C-O bond at positions (2) in GVL can first produce an aldehyde intermediate with hydroxyl and carbonyl groups, and the intermediate can be rapidly hydrogenated to produce 1,4-PDO. Therefore, we do not detect the intermediate during the GVL hydrogenolysis. As mentioned above, the reduction treatment can significantly affect the surface properties of MoO_x-decorated Ni-based catalysts. The catalytic performance of Ni-MoO_x/Al_2O_3 catalysts was studied under different reaction temperatures and hydrogen pressures.

As shown in Table 5, at the low temperature and hydrogen pressure (*i.e.* 160 °C, 3 MPa), altering the reduction temperature from 400 to 600 °C produces 1,4-PDO and 2-MTHF as main products. Especially, GVL conversion over the Ni-MoO_x/Al_2O_3-400 only reaches 15% after a reaction of 4 h, mainly due to the lower amount of active metallic Ni^0 on the catalyst surface. The hydrogenolysis products of GVL are mainly 1,4-PDO, 2-MTHF, VA and PA, with the 1,4-PDO and 2-MTHF selectivities of 43% and 11%, respectively.

The formation of a large amount of VA and PA indicates that hydrogenolysis of GVL can easily happen through the cleavage of the C-O bond either at the position (1) or at the position (2) over the Ni-MoO_x/Al_2O_3-400 catalyst. GVL conversions are significantly boosted over Ni-MoO_x/Al_2O_3-500 and Ni-MoO_x/Al_2O_3-600, indicative of the enhanced catalytic activity due to the presence of more active metallic species. However, there is no obvious relationship between the particle sizes and the catalytic activity of Ni-MoO_x/Al_2O_3 samples, indicating that the textural property of samples and the size of metallic NPs are not key factors affecting the catalytic performance of the present catalyst system. Therefore, the fact that Ni-MoO_x/Al_2O_3-600 catalyst possesses more exposed surface catalytically active Ni^0 species is crucial for achieving a high activity in the GVL hydrogenation. At the same time, the selectivities to 1,4-PDO and 2-MTHF over the Ni-MoO_x/Al_2O_3-600 are increased significantly to about 64% and 28%, respectively. It demonstrates that the hydrogenolysis of GVL at positions (2) and (3) is boosted by increasing reduction temperature for catalyst precursor. Obviously, the reduction treatment at the lower temperature of 400 °C is not effective in the formation of the close Ni^0-defects structure, which should be essential for the hydrogenolysis of C—O and C=O bonds of ester group in GVL. When the hydrogen pressure is increased from 3.0 to 4.0 MPa, both the GVL conversion and the selectivity to 1,4-PDO are remarkably increased over different catalysts (Table 5). Especially, Ni-MoO_x/Al_2O_3-600 yields a higher GVL conversion of 82% with a higher 1,4-PDO selectivity of 78%. With the reaction temperature elevated from 160 to 200 °C, the GVL conversion, as well as the 2-MTHF selectivity, is further increased in each case (Table 5). Especially, high GVL conversions (>90%) can be achieved over Ni-MoO_x/Al_2O_3-500 and Ni-MoO_x/Al_2O_3-600 catalysts. It demonstrates that

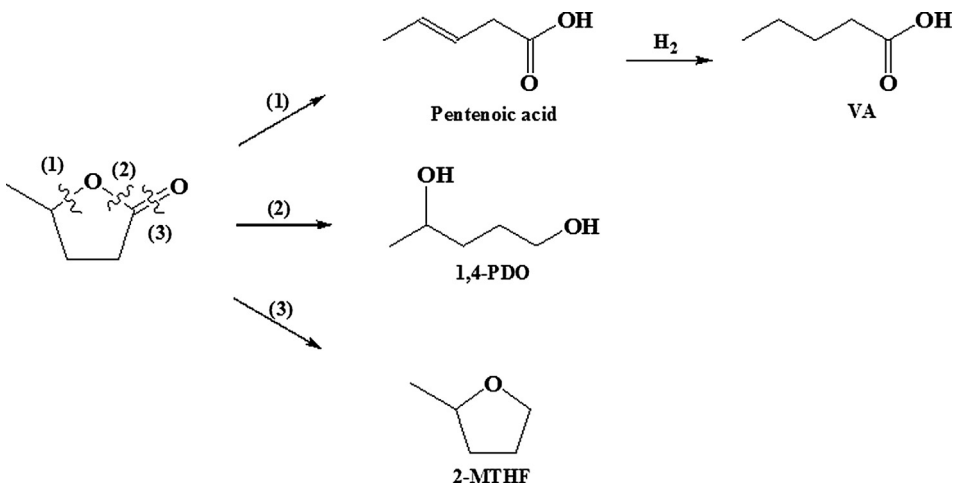

Scheme 1. Reaction pathways for the hydrogenolysis of GVL.

Table 5
Catalytic results for the GVL hydrogenolysis over different catalysts.[a]

Entry	Catalysts	Temp. (°C)	P_{H2} (MPa)	Conv (%)	Selectivity (%)		
					1,4-PDO	2-MTHF	Others [b]
1	Ni-MoO_x/Al_2O_3-400	160	3	15	43	11	46
2	Ni-MoO_x/Al_2O_3-500	160	3	42	65	17	18
3	Ni-MoO_x/Al_2O_3-600	160	3	51	64	28	8
4	Ni/Al_2O_3-500	160	3	27	17	9	74
5	Ni-MoO_x/Al_2O_3-400	160	4	37	57	17	26
6	Ni-MoO_x/Al_2O_3-500	160	4	71	76	15	9
7	Ni-MoO_x/Al_2O_3-600	160	4	82	78	19	3
8	Ni/Al_2O_3-500	160	4	48	31	12	57
9	Ni-MoO_x/Al_2O_3-400	200	4	51	49	29	22
10	Ni-MoO_x/Al_2O_3-500	200	4	90	74	24	2
11	Ni-MoO_x/Al_2O_3-600	200	4	95	68	31	1
12	Ni-MoO_x/Al_2O_3-700	200	4	71	78	20	2
13	Ni/Al_2O_3-500	200	4	80	21	15	64
14	Ni/Al_2O_3-600	200	4	67	21	23	56
15	Ni/Al_2O_3-*im*	200	4	27	34	58	8
16	Ni/MoO_3-*im*	200	4	71	36	24	40
17[c]	MoO_3	200	4	nd	–	–	–
18[d]	Ni/MoO_x-500	160	4	78	61	21	18[e]
19[f]	Ni/MoO_x-500	160	4	70	92	7	1

[a] Reaction conditions: GVL, 10 mmol; catalyst, 0.1 g; mesitylene, 20 ml; time, 4 h.
[b] VA and pentenoic acid as main by-products.
[c] Commercial MoO_3.
[d] Ethanol as the solvent.
[e] Ethyl valerate as main by-product.
[f] H_2O as the solvent.

high reaction temperature is beneficial to the direct cleavage of the C═O bond in GVL. With the increasing reaction time, the GVL conversion over the Ni-MoO_x/Al_2O_3-500 increases gradually (Fig. 7). Meanwhile, the selectivity to 1,4-PDO as the main product first increases and then begins to decrease after a reaction of 4 h, while the selectivity to 2-MTHF increases within 6 h. It illustrates that the route 2 from GVL to 1,4-PDO and the route 3 from GVL to 2-MTHF in Scheme 1 proceed competitively. In comparison, at 200 °C and 4.0 MPa hydrogen pressure, Ni-MoO_x/Al_2O_3-700 delivers a low GVL conversion of about 71% after a reaction of 4 h (Table 5), with the 1,4-PDO and 2-MTHF selectivities of 78 and 20%, respectively. It illustrates that the density of surface metallic Ni should be a key factor in affecting the catalytic activity of the present Ni-based catalysts. On the other side, although Ni/Al_2O_3-500 sample has a much larger specific surface area, total pore volume and average pore diameter than Ni-MoO_x/Al_2O_3, its catalytic activity is still inferior to those of Ni-MoO_x/Al_2O_3 catalysts (Table 5). At the same time, based on the small grain sizes of the present catalyst powders (<7 μm), the internal (or intraparticle) mass transport limitation may be ignored. It demonstrates that there is no obvious correlation between the porosity of samples and their catalytic performance.

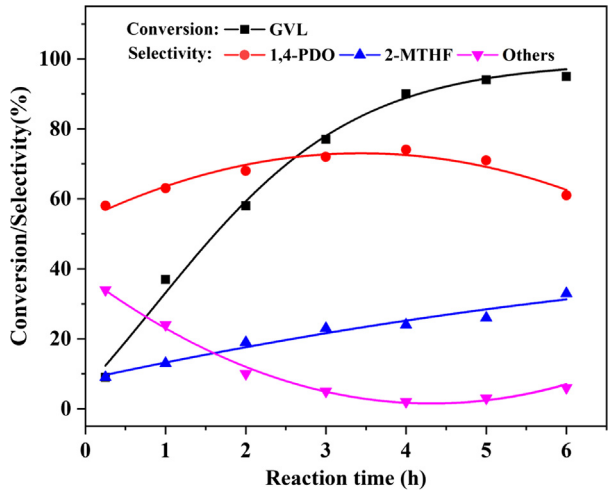

Fig. 7. Change in the conversion and selectivity on the GVL hydrogenolysis with the reaction time over the Ni-MoO_x/Al_2O_3-500 catalyst at a hydrogen pressure of 4.0 MPa and 200 °C.

Further, Ni/Al_2O_3-600 catalyst was prepared by the reduction of NiAl-MMO at 600 °C. It was found that besides low selectivities to 1,4-PDO and 2-MTHF, the catalytic activity of Ni/Al_2O_3-600 was lower than those of Ni/Al_2O_3-500 and Ni-MoO_x/Al_2O_3-600 (Table 5). We also compared the catalytic performance of alumina and molybdenum oxide supported Ni catalysts under the same conditions and found that despite high GVL conversions in some cases, the selectivities to 1,4-PDO and 2-MTHF over Ni/Al_2O_3-500, im-Ni/Al_2O_3, and im-Ni/MoO_3 are much lower than those over Ni-MoO_x/Al_2O_3 catalysts. However, MoO_3 is inactive for the GVL hydrogenolysis (Table 5). Meanwhile, compared with Ni/Al_2O_3-500 with a Ni loading of 66.0 wt%, im-Ni/Al_2O_3 and im-Ni/MoO_3 catalysts with a Ni loading of about 35.0 wt% afford higher selectivity to the total 1,4-PDO and 2-MTHF, mainly due to the presence of more acidic Al_2O_3 and MoO_3 supports [60,61] in catalysts, thus facilitating the cleavage of C═O bond and its adjacent C-O bond in GVL. The results also illustrate that metallic Ni^0 species alone are not highly effective for the cleavage of C—O and C═O bonds of ester group in GVL. In addition, when ethanol is used as the solvent, ethyl valerate also can be produced (Table 5) over the Ni-MoO_x/Al_2O_3-500 through the esterification between VA and ethanol [62]. More interestingly, the 1,4-PDO selectivity can be significantly improved to 92% using H_2O as the solvent (Table 5). Here, the GVL hydrogenolysis in water presents a more sustainable and greener chemical process.

As a result, among tested Ni-based catalysts, Ni-MoO_x/Al_2O_3 catalysts are highlighted as promising catalysts for the synthesis of 1,4-PDO and 2-MTHF from GVL hydrogenolysis. In particular, at the reaction temperature of 200 °C and the relatively low hydrogen pressure of 4.0 MPa, the combined yield of 1,4-PDO and 2-MTHF can reach 94% over the Ni-MoO_x/Al_2O_3-600, reflecting the preferential cleavage of C-O and C═O bonds of ester group in GVL over the C-O bond at the position (1) for GVL hydrogenolysis.

Further, a detailed investigation to determine the effects of reaction temperature and hydrogen pressure on the catalytic reaction was performed utilizing the Ni-MoO_x/Al_2O_3-500. As shown in Fig. 8, the GVL conversion is gradually increased with the elevated reaction temperature, while the combined selectivity of 1,4-PDO and 2-MTHF is increased. When the reaction temperature is elevated to 200 °C, no VA can be obtained. In addition, the low reaction temperature is beneficial to the formation of 1,4-PDO, whereas more 2-MTHF can be formed at higher temperatures. This is because the direct hydrogenation of the carbonyl group in GVL easily occur at higher temperatures. Furthermore, the GVL conversion dramatically increases with the hydrogen pressure increased from 2.0 to 3.0 MPa, and slowly increase with the further increase in the hydrogen pressure. At lower hydrogen pressures, the amount of VA formed accounts for about half of the number of total reaction products. As the hydrogen pressure is gradually elevated to 4 MPa, the VA selectivity decreases rapidly, along with the increased selectivities to 1,4-PDO and 2-MTHF. When the pressure is further increased to 6.0 MPa, the 1,4-PDO selectivity decreases slightly, whereas the 2-MTHF selectivity is slightly improved. The above results indicate a positive effect of hydrogen pressure on the hydrogenolysis of GVL to produce 1,4-PDO and 2-MTHF. Therefore, the reaction temperature of 200 °C and the hydrogen pressure of 4.0 MPa are well-suited for producing 1,4-PDO and 2-MTHF at high total yields. As a result, the formation of 1,4-PDO and 2-MTHF over MoO_x-decorated Ni-based catalysts can be effectively controlled by different reaction conditions (*i.e.* reduction temperature of catalyst precursors, reaction temperature and hydrogen pressure).

3.4. Mechanical study on catalytic reaction

As we know, metallic Ni^0 atoms as catalytically active centres can dissociate molecular hydrogen into active hydrogen species during the GVL hydrogenolysis. In the case of Ni-MoO_x/Al_2O_3 catalysts, the incomplete reduction of Ni^{2+} species at the lower reduction temperature of 400 °C may lead to a relatively low hydrogenolysis activity, while the conversion rate can be enhanced with the reduction temperature for catalyst precursors. On the other side, the XPS characterization of reduced samples reveals that after the reduction of calcined $Mo_7O_{24}^{6-}$ intercalated LDH precursors, large quantities of surface low-valent $Mo^{\sigma+}$ species-oxygen vacancy pairs can be generated. Therefore, to gain more information on the ability for activating GVL on catalysts, two Ni-MoO_x/Al_2O_3-500 and Ni/Al_2O_3-500 samples were characterized by in situ FT-IR of GVL adsorption (Fig. 9). The absorption near 1770 cm^{-1} belongs to the weak chemical adsorption of GVL, while another one near 1745 cm^{-1} is attributed to the C=O stretching vibration [63], indicative of the weakening in the strength of C=O bond in GVL. Noticeably, with the increase in the desorption temperature from 50 °C to 300 °C, the weak GVL adsorption on the Ni-MoO_x/Al_2O_3-500 is gradually weakened and finally completely disappears. However, the absorption peak at 1742 cm^{-1} still almost keeps unchanged at the desorption temperature of 300 °C. For Ni/Al_2O_3-500, the GVL adsorption almost completely disappears when the temperature rises above 200 °C. The much stronger redshift for Ni-MoO_x/Al_2O_3-500 at 1745 cm^{-1} than that for Ni/Al_2O_3-500 clearly demonstrate that Ni-MoO_x/Al_2O_3-500 exhibits stronger adsorption for GVL substrate. In this case, surface MoO_x species can interact with the lone electron pair of oxygen in carbonyl group in GVL, by which the C=O bond or its adjacent C-O bond of ester group can be weakened and finally hydrogenated to 1,4-PDO or 2-MTHF [64–66].

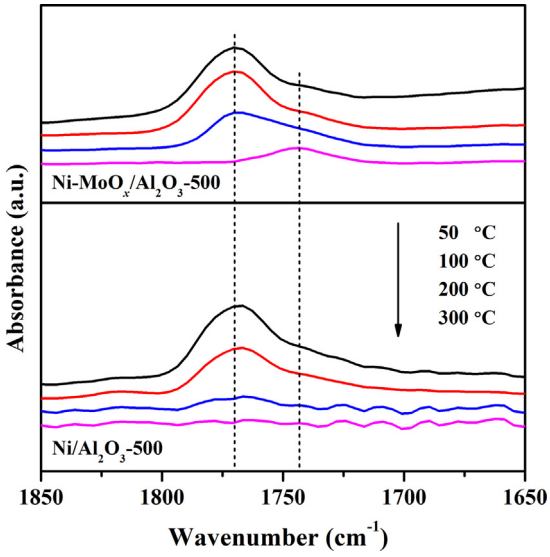

Fig. 9. In situ FT-IR spectra of GVL adsorbed on Ni-MoO_x/Al_2O_3-500 and Ni/Al_2O_3-500 with different desorption temperatures.

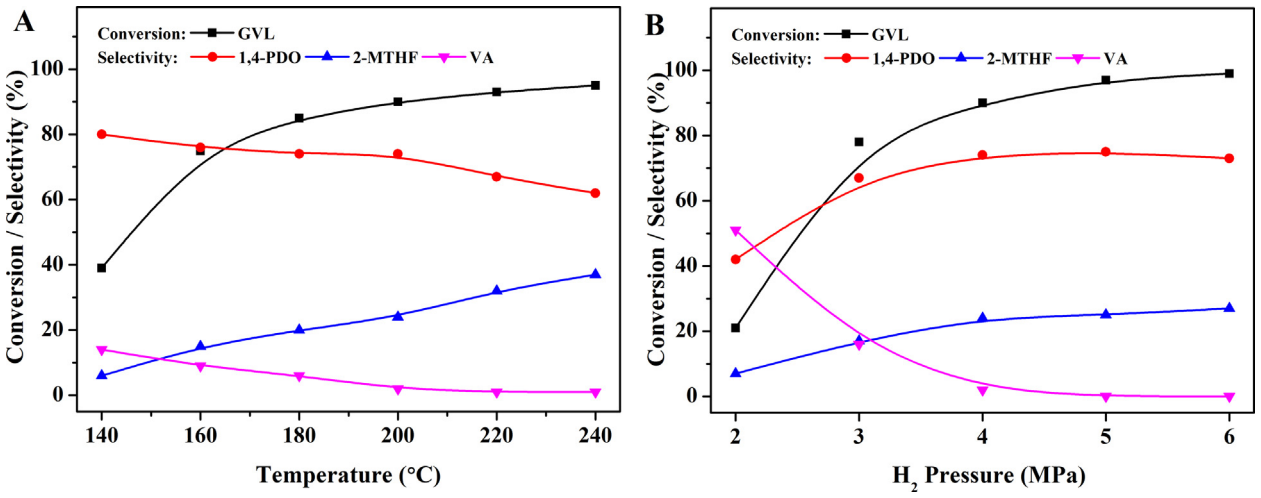

Fig. 8. Effect of the reaction temperature (A) on the GVL hydrogenolysis over the Ni-MoO_x/Al_2O_3-500 catalyst at a hydrogen pressure of 4.0 MPa for 4 h. Effect of the reaction pressure (B) on the GVL hydrogenolysis over the Ni-MoO_x/Al_2O_3-500 catalyst at 200 °C for 4 h.

To investigate the intrinsic nature of catalytically active sites on Ni-based catalysts, the initial turnover frequency of GVL converted (TOF_{GVL}) was calculated based on the moles of GVL converted per mole surface metallic Ni after a short time of 15 min (Table S1). As shown in Table 4, compared with Ni/Al_2O_3-500, $Ni\text{-}MoO_x/Al_2O_3$-500 affords a higher TOF_{GVL} value. Meanwhile, it is noted that the TOF_{GVL} value of $Ni\text{-}MoO_x/Al_2O_3$ catalysts increases gradually with the elevated reduction temperature from 400 to 600 °C. However, further elevating reduction temperature to 700 °C leads to a slight decrease in the TOF_{GVL} value in the case of $Ni\text{-}MoO_x/Al_2O_3$-700. Although the H_2-TPD results demonstrate the occurrence of hydrogen spillover over Ni-based catalysts in the gas phase, active hydrogen species formed on metallic sites through the dissociation of molecular hydrogen can be rapidly quenched by the reactant and abundant mesitylene solvent under the actual liquid phase reaction conditions. Correspondingly, such spillover hydrogen species detected by H_2-TPD in the gas phase would be hardly located on the solid catalyst in the actual liquid phase reaction. Interestingly, the above FT-IR spectra of GVL adsorption reveal that the stronger adsorption of GVL can occur on the $Ni\text{-}MoO_x/Al_2O_3$-500 with abundant oxygen vacancies, compared with Ni/Al_2O_3-500 with surface acidic sites. It implies that during the reaction, GVL molecule may be preferentially adsorbed on surface defective sites acting as adsorption and reaction centers in the cases of $Ni\text{-}MoO_x/Al_2O_3$ catalysts. For Ni/Al_2O_3-500 with a very small amount of surface defects, however, the adsorption of GVL mainly occurs on surface acidic sites. Correspondingly, for $Ni\text{-}MoO_x/Al_2O_3$ catalysts, the formation of more surface oxygen vacancies can greatly facilitate the adsorption of GVL on the surface of catalysts, thereby leading to the higher TOF_{GVL} value. Specially, $Ni\text{-}MoO_x/Al_2O_3$-600 with the highest amount of surface oxygen vacancies (226.2 μmol/g) affords a highest TOF_{GVL} value, despite the smaller density of surface acidic sites on the $Ni\text{-}MoO_x/Al_2O_3$-600 than that on the $Ni\text{-}MoO_x/Al_2O_3$-500. Therefore, the change in the intrinsic activities (TOF_{GVL} values) of $Ni\text{-}MoO_x/Al_2O_3$ catalysts with the amount of surface defects indicates that the present catalytic hydrogenolysis of GVL is a structure sensitive reaction, and the activity of $Ni\text{-}MoO_x/Al_2O_3$ catalysts is closely correlated with the surface defective structure of catalysts.

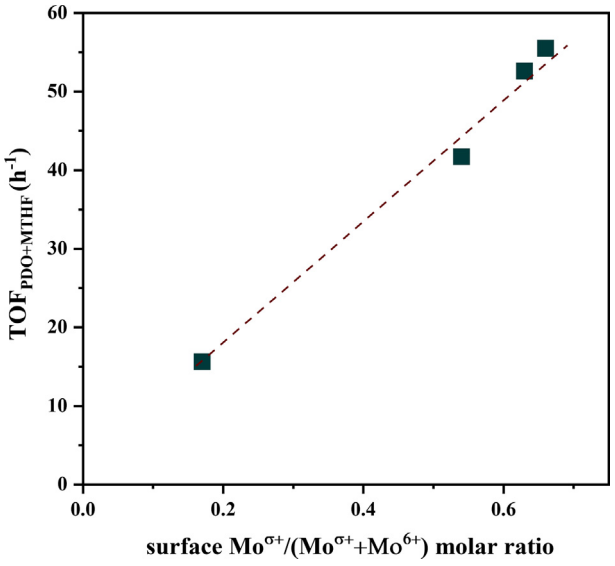

Fig. 10. Change in the initial TOF values of 1,4-PDO and 2-MTHF formed with surface $Mo^{\sigma+}/(Mo^{\sigma+}+Mo^{6+})$ molar ratio over different $Ni\text{-}MoO_x/Al_2O_3$ catalysts.

On the other side, it is noted that the TOF value of 1,4-PDO and 2-MTHF formed ($TOF_{PDO+MTHF}$) over the $Ni\text{-}MoO_x/Al_2O_3$-400 is much lower than those over other Mo-containing catalysts (Table 4). However, Ni/Al_2O_3-500 affords the lowest $TOF_{PDO+MTHF}$ value of 9.0 h^{-1}. Further, as shown in Fig. 10, it is interestingly noted that the $TOF_{PDO+MTHF}$ value over $Ni\text{-}MoO_x/Al_2O_3$ catalysts almost increases linearly with the increase in a surface $Mo^{\sigma+}/(Mo^{\sigma+}+Mo^{6+})$ molar ratio. Specially, compared with other $Ni\text{-}MoO_x/Al_2O_3$ catalysts, $Ni\text{-}MoO_x/Al_2O_3$-700 with the higher fraction of surface defective $Mo^{\sigma+}\text{-}O_v\text{-}Mo^{\sigma+}$ structure afford a higher $TOF_{PDO+MTHF}$ value. It demonstrates that the surface oxygen vacancy should be a key factor controlling selective hydrogenolysis of GVL to form 1,4-PDO and 2-MTHF in the present $Ni\text{-}MoO_x/Al_2O_3$ catalyst system.

The above great changes in the TOF_{GVL} and $TOF_{PDO+MTHF}$ values over Ni-based catalysts strongly illustrate that in addition to metallic Ni atoms as catalytically active sites for dissociating molecular hydrogen, surface defective $Mo^{\sigma+}\text{-}O_v\text{-}Mo^{\sigma+}$ structure over $Ni\text{-}MoO_x/Al_2O_3$ catalysts should play an important role in improving the conversion of GVL and the formation of 1,4-PDO and 2-MTHF in the hydrogenolysis of GVL. Therefore, based on the above characterizations and catalytic experiments, we elucidate the possible picture of the main reaction pathways for the

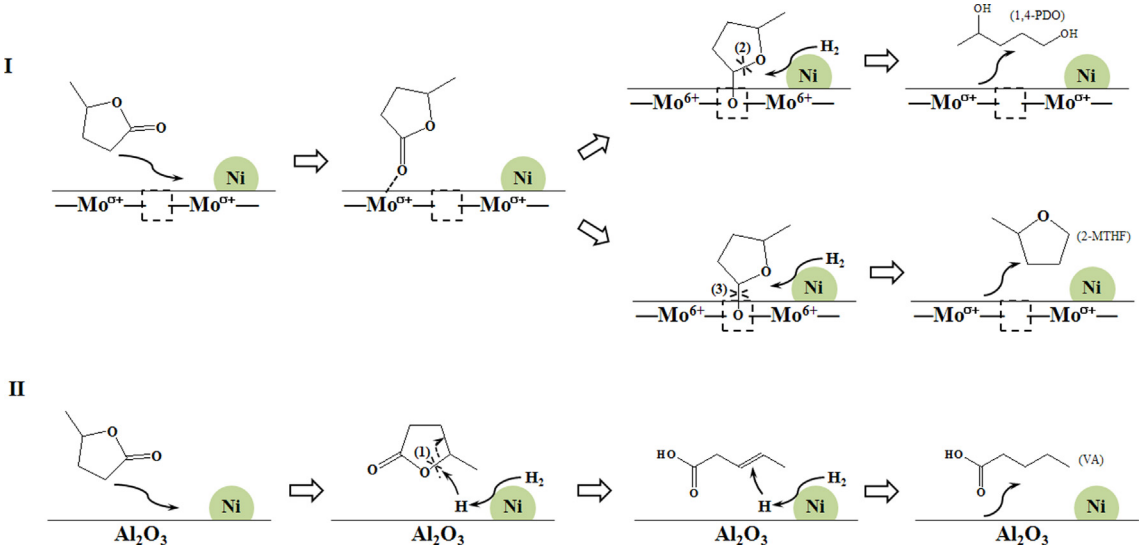

Scheme 2. Proposed reaction mechanisms of GVL hydrogenolysis catalyzed by $Ni\text{-}MoO_x/Al_2O_3$-500 (I) and Ni/Al_2O_3-500 (II).

conversion of GVL over Ni-MoO_x/Al_2O_3 catalysts. As shown in Scheme 2, the oxygen atom of the carbonyl group in GVL can interact with low-valent molybdenum sites on the catalyst surface at the initial reaction stage. Subsequently, GVL molecules are adsorbed at oxygen vacancies. Meanwhile, the coordinatively unsaturated low-valent $Mo^{\sigma+}$ sites linked to neighboring oxygen vacancies can be easily in situ oxidized to high-valent Mo^{6+} species through the electronic delocalization structure and reapportionment of charge. Correspondingly, the oxygen atom of the carbonyl group in GVL molecule occupies the oxygen vacancy and favors the formation of the Mo^{6+}–O–Mo^{6+} structure on the catalyst surface, thus finally activating C═O or C—O moieties. Then, the adjacent metallic Ni species may dissociate molecular hydrogen into active hydrogen species. As-formed hydrogen species participate in the cleavage of the C-O bond or C═O band at positions (2) or (3) of GVL (Scheme 1). At last, 1,4-PDO or 2-MTHF product desorbs from the catalyst surface and the catalyst surface is recovered together with the formation of initial $Mo^{\sigma+}$-O_v-$Mo^{\sigma+}$ defective structure through the redox processes involving cationic Mo species. Correspondingly, surface defects play a crucial role in promoting the GVL hydrogenolysis through the activation of the C═O or C-O bond in GVL, followed by the hydrogenolysis. In a way, large quantities of surface acidic sites and moderate strength acidic sites over Ni-MoO_x/Al_2O_3-500 and Ni-MoO_x/Al_2O_3-600 may be beneficial to the cleavage of C═O bond and its adjacent C-O bond in GVL for producing 1,4-PDO and 2-MTHF.

As a result, in the case of Ni-MoO_x/Al_2O_3 catalysts, abundant surface defective MoO_x species can greatly facilitate the direct cleavage of the C-O bond and C═O bond of ester group in the GVL to produce 1,4-PDO and 2-MTHF. As the reduction temperature increases, increased amounts of surface MoO_x species result in the increased selectivity to 1,4-PDO or 2-MTHF. Due to the lack of interactions between GVL substrate and defective sites, Ni/Al_2O_3-500 gives priority to the GVL hydrogenolysis at the position (1) to generate PA and VA.

4. Conclusions

In summary, a heterogeneous MoO_x-decorated Ni catalyst system was developed to catalyze selective hydrogenolysis of GVL into 1,4-PDO and 2-MTHF. XPS, PAS, and O_2-pulse analysis showed that abundant surface defects (*i.e.* low-valent molybdenum-oxygen vacancy pairs) were constructed on the catalyst surface, and the formation of surface defective structures could be controlled by changing the reduction temperature. Our study showed that Ni-MoO_x/Al_2O_3 catalysts enabled higher selectivities to 1,4-PDO and 2-MTHF in comparison with Mo-free Ni/Al_2O_3 catalyst, and that high reaction temperature and hydrogen pressure were beneficial to selective GVL hydrogenolysis with high combined selectivity of 1,4-PDO and 2-MTHF. A possible mechanism was tentatively proposed, in which the carbonyl group in GVL was adsorbed and activated by surface defective MoO_x species and further hydrogenated to produce 1,4-PDO or 2-MTHF. It was inferred that in the case of Ni-MoO_x/Al_2O_3 catalysts, a cooperative action between active metallic sites and abundant surface defective MoO_x species significantly promoted the hydrogenolysis of GVL and the formation of 1,4-PDO and 2-MTHF. The present findings create an alternative approach to control the surface chemistry of Ni-based catalyst system for highly efficient hydrogenolysis of GVL to form higher value-added chemicals and fuels.

Acknowledgments

We gratefully thank the financial support from National Natural Science Foundation of China (21521005; 21776017).

Appendix A. Supplementary material

Supplementary data to this article can be found online at https://doi.org/10.1016/j.jcat.2019.09.021.

References

[1] A. Corma, S. Iborra, A. Velty, Chemical routes for the transformation of biomass into chemicals, Chem. Rev. 107 (2007) 2411–2502.
[2] H.W. Wijaya, T. Kojima, T. Hara, N. Ichikuni, S. Shimazu, Synthesis of 1,5-pentanediol by hydrogenolysis of furfuryl alcohol over Ni–Y_2O_3 composite catalyst, ChemCatChem 9 (2017) 2869–2874.
[3] W. Li, G. Fan, L. Yang, F. Li, Highly efficient vapor-phase hydrogenation of biomass-derived levulinic acid over structured nanowall-like nickel-based catalyst, ChemCatChem 8 (2016) 2724–2733.
[4] D.M. Alonso, S.G. Wettstein, J.A. Dumesic, Gamma-valerolactone, a sustainable platform molecule derived from lignocellulosic biomass, Green Chem. 15 (2013) 584–595.
[5] K. Yan, Y. Yang, J. Chai, Y. Lu, Catalytic reactions of gamma-valerolactone: A platform to fuels and value-added chemicals, Appl. Catal. B: Environ. 179 (2015) 292–304.
[6] F.D. Pileidis, M.-M. Titirici, Levulinic acid biorefineries: new challenges for efficient utilization of biomass, ChemSusChem 9 (2016) 562–582.
[7] D. Sun, S. Sato, W. Ueda, A. Primo, H. Garciac, A. Corma, Production of C4 and C5 alcohols from biomass-derived materials, Green Chem. 18 (2016) 2579–2597.
[8] D. Sun, Y. Takahashi, Y. Yamada, S. Sato, Efficient formation of angelica lactones in a vapor-phase conversion of levulinic acid, Appl. Catal. A: Gen. 526 (2016) 62–69.
[9] M. Li, G. Li, N. Li, A. Wang, W. Dong, X. Wang, Y. Cong, Aqueous phase hydrogenation of levulinic acid to 1,4-pentanediol, Chem. Commun. 50 (2014) 1414–1416.
[10] M. Pagliaro, R. Ciriminna, H. Kimura, M. Rossi, C.D. Pina, From glycerol to value-added products, Angew. Chem. Int. Ed. 46 (2007) 4434–4440.
[11] J.N. Chheda, G.W. Huber, J.A. Dumesic, Liquid-phase catalytic processing of biomass-derived oxygenated hydrocarbons to fuels and chemicals, Angew. Chem. Int. Ed. 46 (2007) 7164–7183.
[12] X. Du, Q. Bi, Y. Liu, Y. Cao, H. He, K. Fan, Tunable copper-catalyzed chemoselective hydrogenolysis of biomass-derived γ-valerolactone into 1,4-pentanediol or 2-methyltetrahydrofuran, Green Chem. 14 (2012) 935–939.
[13] T. Mizugaki, Y. Nagatsu, K. Togo, Z. Maeno, T. Mitsudome, K. Jitsukawa, K. Kaneda, Selective hydrogenation of levulinic acid to 1,4-pentanediol in water using a hydroxyapatite-supported Pt–Mo bimetallic catalyst, Green Chem. 17 (2015) 5136–5139.
[14] S.C. Patankar, G.D. Yadav, Cascade engineered synthesis of γ-valerolactone, 1,4-pentanediol, and 2-methyltetrahydrofuran from levulinic acid using Pd–Cu/ZrO_2 catalyst in water as solvent, ACS Sustainable Chem. Eng. 3 (2015) 2619–2630.
[15] F.M.A. Geilen, B. Engendahl, A. Harwardt, W. Marquardt, J. Klankermayer, W. Leitner, Selective and flexible transformation of biomass-derived platform chemicals by a multifunctional catalytic system, Angew. Chem. Int. Ed. 49 (2010) 5510–5514.
[16] T. vom Stein, M. Meuresch, D. Limper, M. Schmitz, M. Hoelscher, J. Coetzee, D.J. Cole-Hamilton, J. Klankermayer, W. Leitner, Highly versatile catalytic hydrogenation of carboxylic and carbonic acid derivatives using a Ru-triphos complex: molecular control over selectivity and substrate scope, J. Am. Chem. Soc. 136 (2014) 13217–13225.
[17] W. Li, J.-H. Xie, M.-L. Yuan, Q.-L. Zhou, Ruthenium complexes of tetradentate bipyridine ligands: highly efficient catalysts for the hydrogenation of carboxylic esters and lactones, Green Chem. 16 (2014) 4081–4085.
[18] S. Elangovan, B. Wendt, C. Topf, S. Bachmann, M. Scalone, A. Spannenberg, H. Jiao, W. Baumann, K. Junge, M. Beller, Improved second generation iron pincer complexes for effective ester hydrogenation, Adv. Synth. Catal. 358 (2016) 820–825.
[19] T.J. Korstanje, J.I. van der Vlugt, C.J. Elsevier, B. de Bruin, Hydrogenation of carboxylic acids with a homogeneous cobalt catalyst, Science 350 (2015) 298–302.
[20] D. Srimani, A. Mukherjee, A.F.G. Goldberg, G. Leitus, Y. Diskin-Posner, L.J.W. Shimon, Y.B. David, D. Milstein, Cobalt-catalyzed hydrogenation of esters to alcohols: unexpected reactivity trend indicates ester enolate intermediacy, Angew. Chem. Int. Ed. 54 (2015) 12357–12360.
[21] M.G. Al-Shaal, A. Dzierbinski, R. Palkovits, Solvent-free γ-valerolactone hydrogenation to 2-methyltetrahydrofuran catalysed by Ru/C: a reaction network analysis, Green Chem. 16 (2014) 1358–1364.
[22] Q. Xu, X. Li, T. Pan, C. Yu, J. Deng, Q. Guo, Y. Fu, Supported copper catalysts for highly efficient hydrogenation of biomass-derived levulinic acid and γ-valerolactone, Green Chem. 18 (2016) 1287–1294.
[23] D. Sun, T. Saito, Y. Yamada, X. Chen, S. Sato, Hydrogenation of γ-valerolactone to 1,4-pentanediol in a continuous flow reactor, Appl. Catal. A: Gen. 542 (2017) 289–295.
[24] G. Fan, F. Li, D.G. Evans, X. Duan, Catalytic applications of layered double hydroxides: recent advances and perspectives, Chem. Soc. Rev. 43 (2014) 7040–7066.

[25] D.G. Evans, R.C.T. Slade, Structural aspects of layered double hydroxides, Struct. Bond. 119 (2006) 1–87.
[26] X. Ning, Z. An, J. He, Remarkably efficient CoGa catalyst with uniformly dispersed and trapped structure for ethanol and higher alcohol synthesis from syngas, J. Catal. 340 (2016) 236–247.
[27] W. Li, G. Fan, L. Yang, F. Li, Highly efficient synchronized production of phenol and 2,5-dimethylfuran through a bimetallic Ni-Cu catalyzed dehydrogenation-hydrogenation coupling process without any external hydrogen and oxygen supply, Green Chem. 19 (2017) 4353–4363.
[28] C. Gérardin, D. Kostadinova, N. Sanson, B. Coq, D. Tichit, Supported metal particles from LDH nanocomposite precursors: control of the metal particle size at increasing metal content, Chem. Mater. 17 (2005) 6473–6478.
[29] C. Gérardin, D. Kostadinova, B. Coq, D. Tichit, LDH nanocomposites with different guest entities as precursors of supported Ni catalysts, Chem. Mater. 20 (2008) 2086–2094.
[30] Z. Gao, C. Li, G. Fan, L. Yang, F. Li, Nitrogen-doped carbon-decorated copper catalyst for highly efficient transfer hydrogenolysis of 5-hydroxymethylfurfural to convertibly produce 2,5-dimethylfuran or 2,5-dimethyltetrahydrofuran, Appl. Catal., B: Environ. 226 (2018) 523–533.
[31] G.A. Caravaggio, C. Detellier, Z. Wronski, Synthesis, stability and electrochemical properties of NiAl and NiV layered double hydroxides, J. Mater. Chem. 11 (2001) 912–921.
[32] D. Carriazo, C. Domingo, C. Martín, V. Rives, Structural and texture evolution with temperature of layered double hydroxides intercalated with paramolybdate anions, Inorg. Chem. 45 (2006) 1243–1251.
[33] M. Taibi, S. Ammar, N. Jouini, F. Fiévet, P. Molinié, M. Drillon, Layered nickel hydroxide salts: synthesis, characterization and magnetic behaviour in relation to the basal spacing, J. Mater. Chem. 12 (2002) 3238–3244.
[34] W.G. Hanna, Structural studies of reaction products between paramolybdate anion and some cationic [metal(II) and (III)-(ethylenediamine)$_n$] complexes utilized as new photocatalysts under UV–VIS light illumination, Appl. Catal. B: Environ. 28 (2000) 259–273.
[35] R.L. Frost, A.W. Musumeci, W.N. Martens, M.O. Adebajo, J. Bouzaid, Raman spectroscopy of hydrotalcites with sulphate, molybdate and chromate in the interlayer, J. Raman Spectrosc. 36 (2005) 925–931.
[36] S. Velu, K. Suzuki, M. Vijayaraj, S. Barman, C.S. Gopinath, In situ XPS investigations of $Cu_{1-x}Ni_xZnAl$-mixed metal oxide catalysts used in the oxidative steam reforming of bio-ethanol, Appl. Catal. B: Environ. 55 (2005) 287–299.
[37] C. Zhang, L. Qian, K. Zhang, S. Yuan, J. Xiao, S. Wang, Hierarchical porous Ni/NiO core–shells with superior conductivity for electrochemical pseudo-capacitors and glucose sensors, J. Mater. Chem. A 3 (2015) 10519–10525.
[38] M.J. Ledoux, C.P. Huu, J. Guille, H. Dunlop, Compared activities of platinum and high specific surface area Mo_2C and WC catalysts for reforming reactions: I. catalyst activation and stabilization: Reaction of n-hexane, J. Catal. 134 (1992) 383–398.
[39] F. Solymosi, J. Cserényi, A. Szöke, T. Bánsági, A. Oszkó, Aromatization of methane over supported and unsupported Mo-based catalysts, J. Catal. 165 (1997) 150–161.
[40] D.J. Wang, J.H. Lunsford, M.P. Rosynek, Characterization of a Mo/ZSM-5 catalyst for the conversion of methane to benzene, J. Catal. 169 (1997) 347–358.
[41] M. Anwar, C.A. Hogarth, R. Bulpett, Effect of substrate temperature and film thickness on the surface structure of some thin amorphous films of MoO_3 studied by X-ray photoelectron spectroscopy (ESCA), J. Mater. Sci. 24 (1989) 3087–3090.
[42] F.H.G. Manyar, C. Paun, R. Pilus, D.W. Rooney, J.M. Thompson, C. Hardacre, Highly selective and efficient hydrogenation of carboxylic acids to alcohols using titania supported Pt catalysts, Chem. Commun. 46 (2010) 6279–6281.
[43] J. Yu, Z. Si, L. Chen, X. Wu, D. Weng, Selective catalytic reduction of NO_x by ammonia over phosphate-containing $Ce_{0.75}Zr_{0.25}O_2$ solids, Appl. Catal. B: Environ. 163 (2015) 223–232.
[44] Y. Wang, F. Wang, Y. Chen, D. Zhang, B. Li, S. Kang, X. Li, L. Cui, Enhanced photocatalytic performance of ordered mesoporous Fe-doped CeO_2 catalysts for the reduction of CO_2 with H_2O under simulated solar irradiation, Appl. Catal. B: Environ. 147 (2014) 602–609.
[45] X. Liu, J. Ding, X. Lin, R. Gao, Z. Li, W.-L. Dai, Zr-doped CeO_2 nanorods as versatile catalyst in the epoxidation of styrene with tert-butyl hydroperoxide as the oxidant, Appl. Catal. A: Gen. 503 (2015) 117–123.
[46] X. Liu, K. Zhou, L. Wang, B. Wang, Y. Li, Oxygen vacancy clusters promoting reducibility and activity of ceria nanorods, J. Am. Chem. Soc. 131 (2009) 3140–3141.
[47] M. Kong, Y. Li, X. Chen, T. Tian, P. Fang, F. Zheng, X. Zhao, Tuning the relative concentration ratio of bulk defects to surface defects in TiO_2 nanocrystals leads to high photocatalytic efficiency, J. Am. Chem. Soc. 133 (2011) 16414–16417.
[48] F. Wang, C. Li, X. Zhang, M. Wei, D.G. Evans, X. Duan, Catalytic behavior of supported Ru nanoparticles on the 100}, {110}, and {111 facet of CeO2, J. Catal. 329 (2015) 177–186.
[49] R.G. Kukushkin, O.A. Bulavchenko, V.V. Kaichev, V.A. Yakovlev, Influence of Mo on catalytic activity of Ni-based catalysts in hydrodeoxygenation of esters, Appl. Catal. B: Environ. 163 (2015) 531–538.
[50] M. Ameen, M.T. Azizan, A. Ramli, S. Yusup, M.S. Alnarabiji, Catalytic hydrodeoxygenation of rubber seed oil over sonochemically synthesized Ni-Mo/γ-Al_2O_3 catalyst for green diesel production, Ultrason. Sonochem. 51 (2019) 90–102.
[51] M. Saghafi, S. Heshmati-Manesh, A. Ataie, A.A. Khodadadi, Synthesis of nanocrystalline molybdenum by hydrogen reduction of mechanically activated MoO_3, Int. J. Refract. Met. Hard Mater. 30 (2012) 128–132.
[52] T. Borowiecki, W. Gac, A. Denis, Effects of small MoO_3 additions on the properties of nickel catalysts for the steam reforming of hydrocarbons: III. reduction of Ni-Mo/Al_2O_3 catalysts, Appl. Catal. A: Gen. 270 (2004) 27–36.
[53] A.S. Martensson, C. Nyberg, S. Andersson, Adsorption of hydrogen on a stepped nickel surface, Surf. Sci. 205 (1988) 12–24.
[54] B. Liu, M.T. Lusk, J.F. Ely, Influence of nickel catalyst geometry on the dissociation barriers of H_2 and CH_4:Ni_{13} versus Ni (111), J. Phys. Chem. C 113 (2009) 13715–13722.
[55] Y. Cesteros, P. Salagre, F. Medina, J.E. Sueiras, Synthesis and characterization of several Ni/$NiAl_2O_4$ catalysts active for the 1,2,4-trichlorobenzene hydrodechlorination, Appl. Catal. B: Environ. 25 (2000) 213–227.
[56] F. Yang, D. Liu, Y. Zhao, H. Wang, J. Han, Q. Ge, X. Zhu, Size dependence of vapor phase hydrodeoxygenation of m-cresol on Ni/SiO_2 catalysts, ACS Catal. 8 (2018) 1672–1682.
[57] P. Sun, G. Gao, Z. Zhao, C. Xia, F. Li, Stabilization of cobalt catalysts by embedment for efficient production of valeric biofuel, ACS Catal. 4 (2014) 4136–4142.
[58] T. Pan, J. Deng, Q. Xu, Y. Xu, Q.-X. Guo, Y. Fu, Catalytic conversion of biomass-derived levulinic acid to valerate esters as oxygenated fuels using supported ruthenium catalysts, Green Chem. 15 (2013) 2967–2974.
[59] J.C. Serrano-Ruiz, D. Wang, J.A. Dumesic, Catalytic upgrading of levulinic acid to 5-nonanone, Green Chem. 12 (2010) 574–577.
[60] P.J. Chupas, K.W. Chapman, G.J. Halder, Elucidating the structure of surface acid sites on γ-Al_2O_3, J. Am. Chem. Soc. 133 (2011) 8522–8524.
[61] Sh.O. Omarov, E.A. Vlasov, D.A. Sladkovskiy, K.V. Semikin, A.N. Matveyeva, S.P. Fedorov, G.V. Oganesyan, D.Yu. Murzin, Physico-chemical properties of MoO_3/ZrO_2 catalysts prepared by dry mixing for isobutane alkylation and butene transformations, Appl. Catal. B: Environ. 230 (2018) 246–259.
[62] N. Scotti, M. Dangate, A. Gervasini, C. Evangelisti, N. Ravasio, F. Zaccheria, Unraveling the role of low coordination sites in a Cu metal nanoparticle: a step toward the selective synthesis of second generation biofuels, ACS Catal. 4 (2014) 2818–2826.
[63] M.A. Centeno, M. Montes, J. Fernandez-Sanz, J.A. Odriozola, DRIFTS study of acetone adsorption over AIPON catalysts, Mater. Sci. Forum 383 (2002) 105–110.
[64] P. Reyes, C. Rodríguez, G. Pecchi, J.L.G. Fierro, Promoting effect of Mo on the selective hydrogenation of cinnamaldehyde on Rh/SiO_2 catalysts, Catal. Lett. 69 (2000) 27–32.
[65] Q. Hu, L. Yang, G. Fan, F. Li, Hydrogenation of biomass-derived compounds containing a carbonyl group over a copper-based nanocatalyst: Insight into the origin and influence of surface oxygen vacancies, J. Catal. 340 (2016) 184–195.
[66] Z. Gao, L. Yang, G. Fan, F. Li, Promotional role of surface defects on carbon-supported ruthenium-based catalysts in the transfer hydrogenation of furfural, ChemCatChem 8 (2016) 3769–3779.